Parasitic Layer-Based Radiation Pattern Reconfigurable Antenna for 5G Communications

Mohammad Ababil Hossain, Israfil Bahceci, *Member, IEEE*, and Bedri A. Cetiner, *Member, IEEE*

***Abstract*— The design, prototyping, and characterization of a radiation pattern reconfigurable antenna (RA) targeting 5G communications are presented. The RA is based on a reconfigurable parasitic layer technique in which a driven dipole antenna is located along the central axis of a 3-D parasitic layer structure enclosing it. The reconfigurable parasitic structure is similar to a hexagonal prism, where the top/bottom bases are formed by a hexagonal domed structure. The surfaces of the parasitic structure house electrically small metallic pixels with various geometries. The adjacent pixels are connected by PIN diode switches to change the geometry of the parasitic surface, thus providing reconfigurability in the radiation pattern. This RA is designed to operate over a 4.8–5.2 GHz frequency band, producing various radiation patterns with a beam-steering capability in both the azimuth ($0° < \phi < 360°$) and elevation planes ($-18° < \theta < 18°$). Small-cell access points equipped with RAs are used to investigate the system level performances for 5G heterogeneous networks. The results show that using distributed mode optimization, RA equipped small-cell systems could provide up to 29% capacity gains and 13% coverage improvements as compared to legacy omnidirectional antenna equipped systems.**

***Index Terms*— 5G, antenna radiation patterns, beam-steering, cellular radio, heterogeneous networks, parasitic antennas, reconfigurable antennas (RAs), small-cell.**

I. Introduction

5G WIRELESS communications systems are creating a paradigm shift for wireless services compared to 4G and earlier predecessors. Challenging capacity, coverage, and latency requirements [1] under a plethora of use-case scenarios with vastly different user and traffic loads mandate a thorough system design. Small cell concepts and advanced multi-input multi-output (MIMO) antennas are key approaches that can meet the performance requirements of 5G systems. However, satisfying these requirements with low power, low cost, and complexity is challenging when MIMO systems use a large number of legacy single-function antennas. As a single reconfigurable antenna (RA) can perform multiple functions by dynamically changing its properties (frequency, radiation pattern, and polarization), it can replace multiple single-function legacy antennas thereby resulting in lower power consumption and lower system cost [2]–[4]. Also, dynamically reconfigurable properties of an RA can be used as important additional degrees of freedom in an adaptive system, resulting in significant gains [5].

There are various approaches and enabling technologies in developing RAs [2]. Pixel antennas, also known as reconfigurable apertures, divide the radiating antenna region into a number of electrically small segments, called pixels, which are interconnected by means of switching, i.e., PIN diodes, MEMS, and so on [6], [7]. By exciting different switch configurations, the antenna architecture is reshaped, thus reconfiguring its frequency and radiation properties. In this paper, a 3-D radiation pattern RA is presented where a single driven dipole antenna is enclosed by a 3-D reconfigurable parasitic layer. In this approach, the driven antenna region remains unmodified while a parasitic structure placed in the near-field region of the driven antenna is discretized into a number of pixels [3], [8]. The parasitic layer structure is similar to a hexagonal prism in which the top and bottom bases of the prism are formed by hexagonal domes. The driven dipole lies along the central axis of the prism. The surfaces of the parasitic structure house electrically small metallic pixels with various geometries. This RA is designed to operate in the 5 GHz band ($4.8 < f < 5.2$ GHz) and is capable of producing a large number of different radiation patterns including dipole patterns with up/down elevation tilts, and patch antenna patterns that can be steered in both the azimuth ($0° < \phi < 360°$) and elevation planes ($-18° < \theta < 18°$).

A close relative of the RA presented in this paper is the electronically steerable passive array radiator (ESPAR) antenna [9]. ESPAR antennas are generally capable of yielding steerable directive patterns in azimuth plane [10]–[12], where $\sim\lambda/4$ distance between the central active antenna element and surrounding parasitic elements is needed. This makes ESPAR larger than the presented RA for which this distance is around $\lambda/6$. To introduce beam-steering in the elevation plane, which is limited to the upper hemisphere, i.e., above ground plane, an ESPAR antenna requires a ground plane with variable dimensions [9], [13]. The RA presented in this paper can perform beam-steering in a large portion of the 3-D space corresponding to ($0° < \phi < 360°$) and ($-18° < \theta < 18°$).

Traditionally, the antenna and adaptive signal processing fields have been treated as dichotomous fields, thus limiting the optimal design space that could be explored for significant performance improvement. The RA of this paper generates various radiation patterns that can effectively be used in 5G systems where spatial distribution of user and traffic loads may

Manuscript received October 31, 2016; revised August 14, 2017; accepted September 11, 2017. Date of publication September 29, 2017; date of current version November 30, 2017. This work was supported by AFOSR under Grant FA 9550-15-1-0040 DEF. *(Corresponding author: Israfil Bahceci.)*

The authors are with the Department of Electrical and Computer Engineering, Utah State University, Logan, UT 84322 USA, and also with i5 Technologies, Inc., North Logan, UT USA (e-mail: ababil.hossain@usu.edu; bahceci@usu.edu; bedri.cetiner@usu.edu).

Color versions of one or more of the figures in this paper are available online at http://ieeexplore.ieee.org.

Digital Object Identifier 10.1109/TAP.2017.2757962

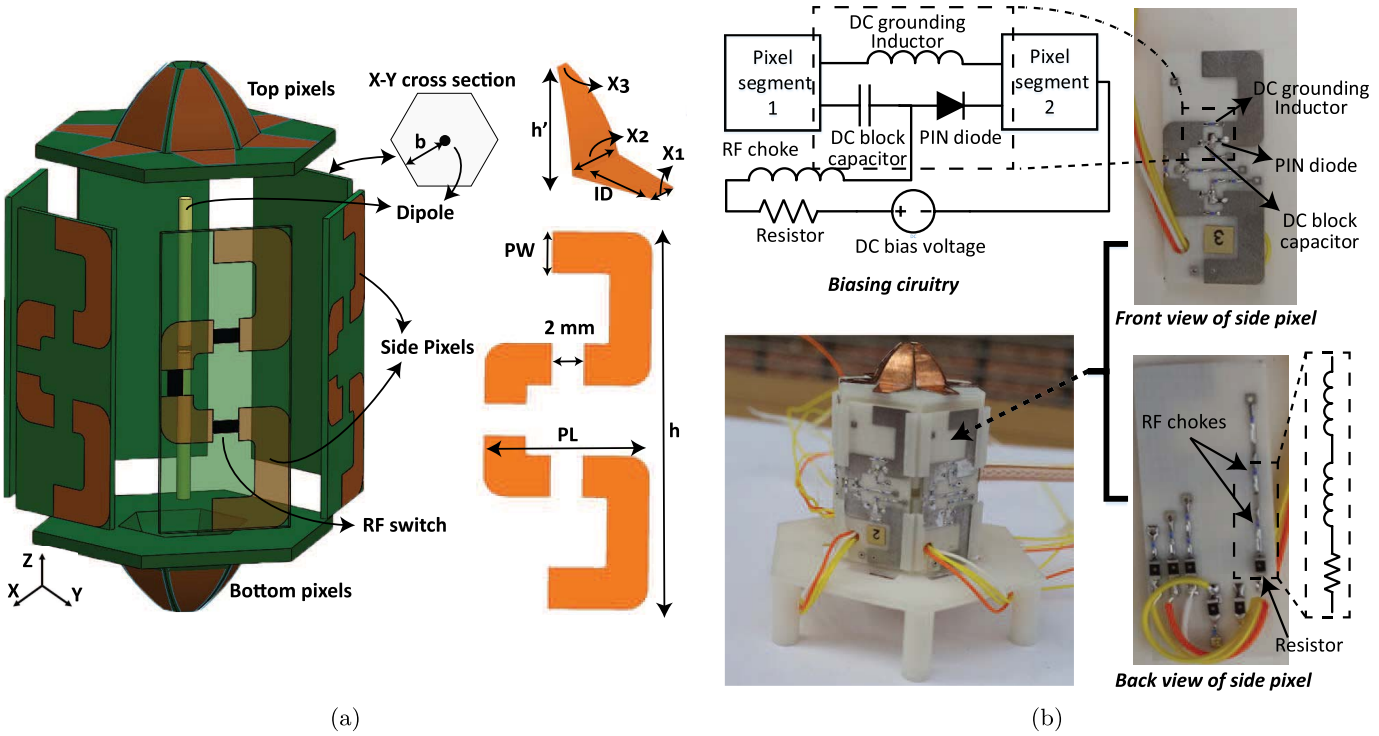

Fig. 1. (a) Schematics of the RA. (b) Photograph of the fabricated prototype: front view of rectangular PCB face with pixels and switching circuitry and back view of rectangular PCB face with bias lines. Dimensions (in mm): $b = 10$, $PL = 10$, $PW = 2.5$, $h = 23$, $h' = 5.5$, $ID = 5$, $X_1 = 2.5$, $X_2 = 5$, and $X_3 = 1$.

vary over time in 3-D space [14], [15]. Ultradense small cell deployment requires low-cost access point equipment and can achieve high capacity and coverage performance by exploiting 3-D beam-steering capability of the low-cost single-element RA of this paper. To quantify potential gains, the system level performance of a typical 5G heterogeneous network in which femto cell access points (FAPs) are equipped with the presented RA is investigated. A low-complexity and low-overhead distributed mode selection scheme that can determine the appropriate RA mode in response to changes in the channel and user density is proposed. The results show that the RA equipped FAPs with minimal complexity and overhead could achieve up to 29% capacity and 13% coverage improvements compared to legacy omnidirectional antenna equipped small cell systems. Our efforts in this paper, in a sense, are a step forward in developing a unified approach, where antenna design, communications/signal processing and network aspects are seamlessly integrated, and all system parameters (environment, EM wave properties, and communication algorithms) are jointly optimized. This approach is key to achieve the throughput and coverage performance required for 5G and beyond communication systems.

II. Antenna Structure and Its Operating Principle

A. Antenna Structure

The main components of the RA structure are the driven dipole and the surrounding 3-D reconfigurable parasitic layer with interconnecting switches and biasing circuitry as depicted in Fig. 1.

1) Driven Antenna: A half-wave length dipole with an impedance bandwidth covering the 4.8–5.2 GHz frequency range is used as the driven antenna. It is designed by using a full-wave EM analysis tool [16] and is constructed using a coaxial cable (Amphenol RF, RG-316/U), where a very small feed-gap of 0.15 mm is kept between the dipole arms to reduce the quadrature component of current that can negatively affect resonance [17]. The full-wave EM model of the dipole is used to design the parasitic layer, where the pixel geometries and switching circuitry are jointly optimized in obtaining the targeted modes of operations corresponding to various radiation patterns.

2) Parasitic Layer and Pixels: The geometry of the 3-D parasitic layer structure, which encloses the driven dipole antenna located along the central axis, is similar to a hexagonal prism, which can be classified as octahedron with eight faces. The top and bottom bases of the prism are formed by identical hexagonal domes and the six side faces are formed by rectangular-shaped planes. As shown in Fig. 1, the surfaces of the eight faces have electrically small metallic pixels with various geometries, and the adjacent pixels are interconnected by PIN diode switches.

The construction of parasitic layer involves two steps. First, a mechanical supporting structure, which consists of top, bottom, and intermediate parts are 3-D printed and assembled together. The material used is acrylonitrile-butadiene-styrene ($\epsilon_r = 2.1, \tan\delta = 0.05$). Next, the parasitic pixels are built. The pixels of the intermediate part that consists of six rectangular faces are formed on separate rectangular-shaped microwave laminates, ($\epsilon_r = 3.35, \tan\delta = 0.0025$)

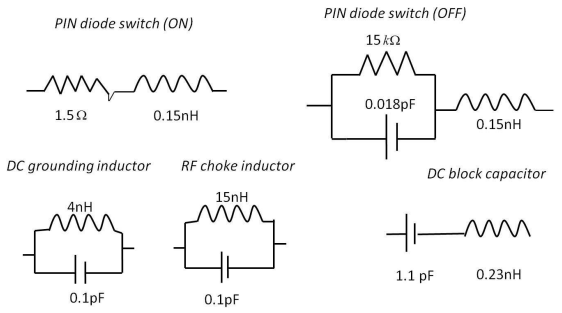

Fig. 2. Equivalent circuit models of the lumped components and PIN diode.

with a thickness of 0.5 mm by using typical printed circuit board (PCB) processes. Each of these six rectangular shaped microwave laminates with metallic parasitic pixels and associated switching circuitry are slid into each of the grooved faces of the supporting 3-D printed structure. As shown in Fig. 1, a spiral shape is divided into three smaller metallic pixels for each rectangular face. Each of the hexagonal domes comprising the top and bottom parts of the supporting structure contains six conformal curved pixels. These pixels are first constructed by mechanically shaping copper metal sheets and then bonded on to the surface of the domes. The reconfigurability of the radiation pattern over the horizon ($0° < \phi < 360°$) is mainly controlled by the pixels of the intermediate part, while the beam tilting over elevation angles ($-18° < \theta < 18°$) is controlled by the top and bottom pixels. Notice that the dome structure has a flat surface region that houses the switching circuitry interconnecting the pixels of top and bottom parts to those of the intermediate part.

3) Switching Circuitry: PIN diodes are used to interconnect adjacent pixels. The biasing scheme, which is similar to the one used in [18], is shown in Fig. 1, where all pixels are mutually connected by dc grounding inductors. The anode of each PIN diode switch is connected to one pixel and its cathode is connected through a dc-block capacitor to the adjacent pixel. The biasing lines are located on the back side of the rectangular-shaped microwave laminates and are split in short nonresonant sections by means of RF chokes to minimize their coupling with the pixels as shown in Fig. 1(b). The manufacturer details and properties of the PIN diode and surface-mount device (SMD) lumped components are shown in Table I. Typically, 1 V dc power supply on the PIN diode would be sufficient to turn on the switch, while 0 V will keep the switch in OFF status. The equivalent circuit models of these lumped components are obtained using their scattering parameters provided by the manufacturers and are shown in Fig. 2. These models are used in the design of the RA.

B. Working Mechanism

The working mechanism of this RA is similar to and can be explained by traditional Yagi-Uda array principle [19]. The dipole acts as the driven element. The electrical length of the connected/disconnected pixels, i.e., parasitic elements, of the 3-D parasitic layer determines whether they work as directors or reflectors. When the overall electrical length of any

TABLE I
SMD COMPONENTS USED IN SWITCHING CIRCUITRY

Component model	Manufacturer	Device	Value	SRF (GHz)
MA4AG910 PIN diode	MACOM	RF switch	NA	NA
LQP03TN 4N0B02D	Murata Electronics	DC grounding inductor	4nH	5.3
LQP03TN 15NH02D	Murata Electronics	RF chokes inductor	15nH	5.3
GRM0225C1 H1R1WA03L	Murata Electronics	DC block capacitor	1.1pF	10

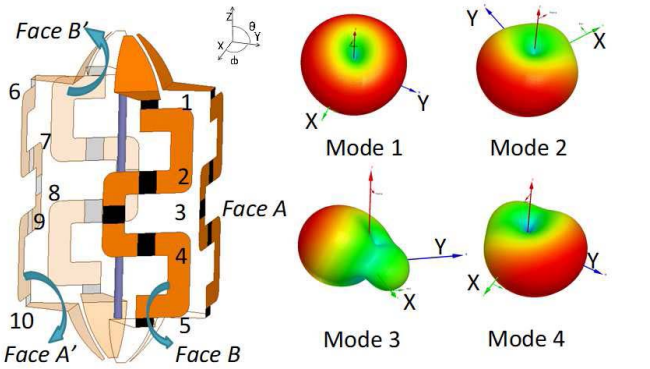

Switch ID		1	2	3	4	5	6	7	8	9	10
Mode 1	A/A′	0	0	0	0	0	0	0	0	0	0
Mode 2	B/B′	0	1	1	1	0	0	0	0	0	0
Mode 3	B/B′	0	0	1	1	1	1	0	0	0	0
Mode 4	A/A′	0	0	0	0	0	0	1	1	1	0
	B/B′	0	0	0	0	0	0	1	1	1	0

Fig. 3. Switch configuration for various modes of operation. For clarity, four faces of the hexagonal structure are explicitly depicted. The pixels on the other two faces are disconnected. The table indicates the switch states for Modes 1–4, with 0 and 1 denoting OFF and ON states, respectively.

connected pixels becomes greater than $\lambda/2$ at the resonance frequency, that portion starts to work as a reflector. For lengths less than $\lambda/2$, the parasitic element works as a director.

This RA is capable of generating various radiation patterns which can be classified under four cases that are illustrated in Fig. 3.

1) Omni-Directional Mode: When all the switches are kept at their OFF state, the individual pixels are electrically short enough to be transparent to the radiated fields of the driven dipole, from which the omni-directional dipole pattern is obtained.

2) Azimuthal Beam-Steering Modes: These are similar to patch antenna pattern, where the main beam direction is steered in the azimuth over six different directions corresponding to main beam directions $\phi \in \{30°, 90°, \ldots, 330°\}$. For a given beam-steering direction, the pixels on the surface of rectangular-shaped face to which the beam-steering direction is normal are disconnected while the pixels on the diametrically opposite surface are all connected. The parasitic layer with connected pixels becomes electrically long enough to work as a reflector.

3) Elevation Beam-Steering Modes: Similar to the patterns of azimuthal modes, the beam-steering can be performed in the elevation plane as well. The typical beam-steering range is $-18° < \theta < 18°$. For the azimuthal beam-steering, the axis, which runs from the reflector to the director, is in the azimuth plane (x–y plane) and is directed toward the beam-steering direction. However, for elevation beam-steering, this axis is tilted and directed along the direction of elevation beam-steering angle. To this end, the pixel of the top (or bottom) dome is connected to the adjacent first top (or bottom) pixel of the intermediate part of the parasitic layer to form the director. The reflector is formed by connecting the pixel of the bottom (or top) dome with the adjacent two bottom (or top) pixels, which are located on the diametrically opposite face with respect to the director face. Therefore, the beam can be steered in both upper and lower elevation planes. For example, in order to create a downtilted beam toward Face A (see Fig. 3), switch 5 on Face A and switches 6, 7, and 8 on Face A' are turned ON, while an uptilted beam toward Face A would require switch 1 on Face A and switches 8, 9, and 10 on Face A' to be turned ON.

4) Modified Dipole Pattern Modes (Diversity Modes): This RA generates other radiation patterns that can be categorized as modified dipole patterns or diversity patterns. Some of these patterns are obtained by combining the interconnecting switch statuses of the above given three cases. For example, if the pixels of faces A and B are disconnected to form the directors, while the pixels of the diametrically opposite faces (faces A' and B') are all connected forming the reflectors, the resulting beam-steering angle is obtained by the vector sum of azimuthal beam-steering directions corresponding to the modes of A & A' and B & B'. One such example, Mode 4, is shown in Fig. 3. As is demonstrated in the system level performance section of this paper, some of these diversity modes may be the winning modes yielding the best system level performances in terms of throughput and coverage for a given communication scenario.

III. Optimization Of 3-D RA Structure and Switching Circuitry

The overall antenna structure including the geometrical shape and dimensions of the parasitic layer along with those of the pixels and switching circuitry have been jointly optimized in two steps. First, the 3-D parasitic layer's geometry and dimensions have been optimized, where the switch ON and OFF states are taken as perfect short and open circuits, respectively. In the second phase, the components of the switching circuitry, namely, PIN diode, dc-block capacitor, RF choke inductor, and dc grounding inductor properties [the values of capacitance, inductance, and self-resonant-frequencies (SRFs)] used at the parasitic layer are properly determined as these components play roles on the performances of the targeted radiation pattern modes.

A. Optimization of 3-D Parasitic Layer

The main design parameters are pixel length, PL, pixel width, PW, the distance from the central axis to any of the six rectangular faces, b, and pixel height, h, as shown in Fig. 1(a). These dimensions and pixel shape are determined by optimizing the azimuthal beam-steering performance of the RA. The individual pixel shapes are obtained by dividing a spiral shape geometry at three strategic locations, thereby only three PIN diode switches are needed for each rectangular face of the parasitic layer. Spiral geometry as opposed to straight rectangular strip geometry is chosen as it provides longer electrical path for the current.

TABLE II
Impact of PL and b on the Realized Gain and Front-to-Back Ratio

PL and b (mm)	PW (mm)	Resonance Frequency (GHz)	Maximum gain (dBi)	front to back ratio (dB)
8	2	5.1	4.2	5.3
10	2	5.1	3.7	4.1
12	2	5.1	3.4	3.3
8	2.5	5.0	4.8	7.3
10	2.5	5.1	4.1	5.1
12	2.5	5.1	3.5	3.7

First, h is fixed at 23 mm symmetric about the dipole center. Then PL, PW, and b, are optimized. In Fig. 4, the effect of variation of PL, b, and PW on the impedance bandwidth and azimuthal beam-steering mode radiation characteristics of the RA is shown. The results are summarized and compared in Table II. It is seen that a smaller b value results in improved resonance bandwidth, gain, and front-to-back ratio. In addition, an increase in PW results in higher gain and front-to-back ratio levels. The jointly optimized values for PL, b, and PW are determined to be 10, 10, and 2.5 mm, respectively.

The base of the dome structure is kept smaller than the original hexagon base of the hexagonal prism to accommodate the switch circuitry that connects the pixels of the top and bottom dome surface with those of the intermediate part. The top view of the dome structure is shown in Fig. 1(a), where the distance from the edge of the dome base to the outer edge of the hexagon base is chosen as $ID = 5$ mm. The geometry and pixel dimensions of the dome surfaces, which are optimized to improve elevation beam-steering capability, are found as $x_1 = 2.5$ mm, $x_2 = 5$ mm, $x_3 = 1$ mm, and $h' = 5.5$ mm. Notice that for the sake of simplicity the ON/OFF switch states for the top and bottom parts are used as perfect short/open circuit.

B. Determination of SMD Components

By using the RA dimensions determined in the first step, the PIN diode, dc-block capacitor, RF choke inductor, and dc grounding inductor are chosen. The SRF of the RF choke is chosen to be around 5.3 GHz, thus RF chokes would appear as high impedance in the 5 GHz band. Inductors are also used as dc grounding elements and are placed in between all pixels. In this manner, all the pixels can be dc grounded together to provide ground for dc biasing purpose. The SRF of these inductors was chosen to be the same value as RF chokes.

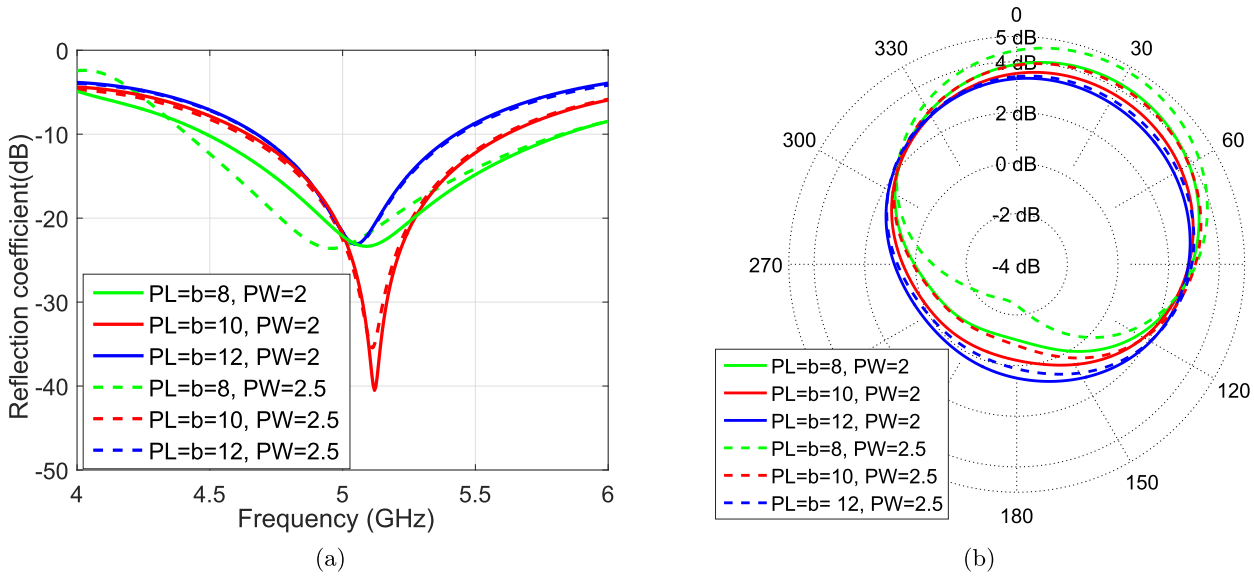

Fig. 4. (a) Reflection coefficient (S_{11}). (b) Realized gain in azimuth plane at $\theta = 90°$ for various PW, PL and b values.

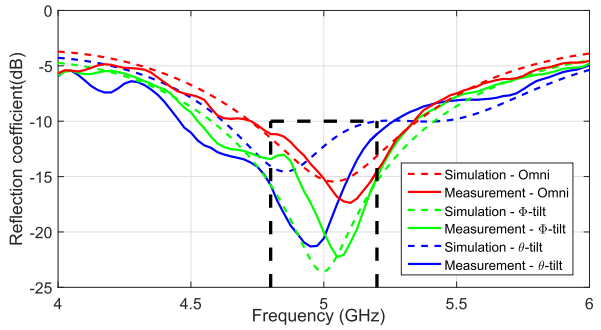

Fig. 5. Comparison of the reflection coefficients (S_{11}) from the full-wave analysis and those from the measurements using the prototype having the PIN diode-based switching circuitry.

DC block capacitors are used to properly bias the PIN diode switches as shown in Fig. 2. The dc block capacitor is selected so that it has a low RF impedance in the 5 GHz band. These values are given in Table I.

IV. Numerical Results

A. Simulation and Measurements

We have chosen three different types of radiation pattern modes, which are omni-directional mode, azimuthal beam-steering mode, and elevation beam-steering mode to present the impedance and radiation characteristics. As shown in Fig. 5, the measured and simulated reflection coefficient results agree very well. It is worth noting that maintaining the impedance matching while the radiation pattern is configured is one of the main challenges of RA design. As seen in Fig. 5, common bandwidth from 4.8 to 5.2 GHz exists for the three modes of operation.

In Fig. 6(a), the simulated realized gain patterns corresponding to six different modes of azimuthal beam-steering ($\phi \in \{30°, 90°, 150°, \ldots, 330°\}$) (corresponding to the Mode-2 indicated in Fig. 3), along with the pattern of omni-directional mode (Mode-1 in Fig. 3) in x–y plane are shown. The maximum realized gain in the steered beam direction is ∼4.9 dBi, where the 3-dB beamwidth is ∼110°. The front-to-back ratio of these patterns is ∼7 dB. Fig. 6(a) also includes the measured radiation patterns for omni-direcitonal mode and the azimuth beam-steering mode at $\phi = 30°$, which are in good agreement with the corresponding full-wave analysis results. In Fig. 6(b), the simulated realized gain patterns corresponding to four different modes of elevation beam-steering $\theta_{\text{tilt}} \in \{-18°, 18°\}$ for $\phi = 30$ and 210°, and the measured pattern for $\theta_{\text{tilt}} = 18°$ at $\phi = 30°$ plane are shown. It is again seen that the measured pattern is in good agreement with the full-wave analysis result.

B. Radiation Pattern RA for Wireless Heterogeneous Network

1) System Model: We consider a ultra-dense heterogenous network of K base stations (eNBs), each of which has S sectors and $L \gg K$ FAPs [20], [21]. Let $\mathcal{B} = \{B_{s+(k-1)S}, k = 1, \ldots, K, s = 1, \ldots, S\}$ and $\mathcal{F} = \{F_l, l = 1, \ldots, L\}$, denote the set of all eNB sectors and FAPs, respectively. User-i, U_i, $i \in \mathcal{U} \triangleq \{1, \ldots, U\}$ may be served by one of the eNB sectors or FAPs. Let $X_j \in \mathcal{X} \triangleq \{\mathcal{B} \cup \mathcal{F}\}$ denote the serving station for U_i. Furthermore, let $\mathcal{U}_j = \{j_1, \ldots, j_{|\mathcal{U}_j|}\} \subseteq \mathcal{U}$ denote the set indices of the users being served by X_j.

It is assumed that the antenna radiation pattern at B_k is fixed whereas FAPs are equipped with the RA antenna elements that can dynamically be switched. Each user is assumed to have omni-directional (standard half-wavelength dipole) antennas. Let us denote the complex e-field radiation patterns at B_k, F_l and U_i by $\vec{B}_j(\theta, \phi; \nu)$, $\vec{A}_l(\theta, \phi; \mu)$, and $\vec{G}_i(\theta, \phi)$, respectively, where $\nu \in \mathcal{M}_B \triangleq \{1, \ldots, M_B\}$ for B_j, and $\mu \in \mathcal{M}_F \triangleq \{1, \ldots, M_F\}$ for F_l, denotes the indices of the selected antenna pattern at B_j, and the RA excited mode at F_l, respectively. The wireless channel, $h_{i,j}(\eta_j)$, from transmit station X_j to receiver

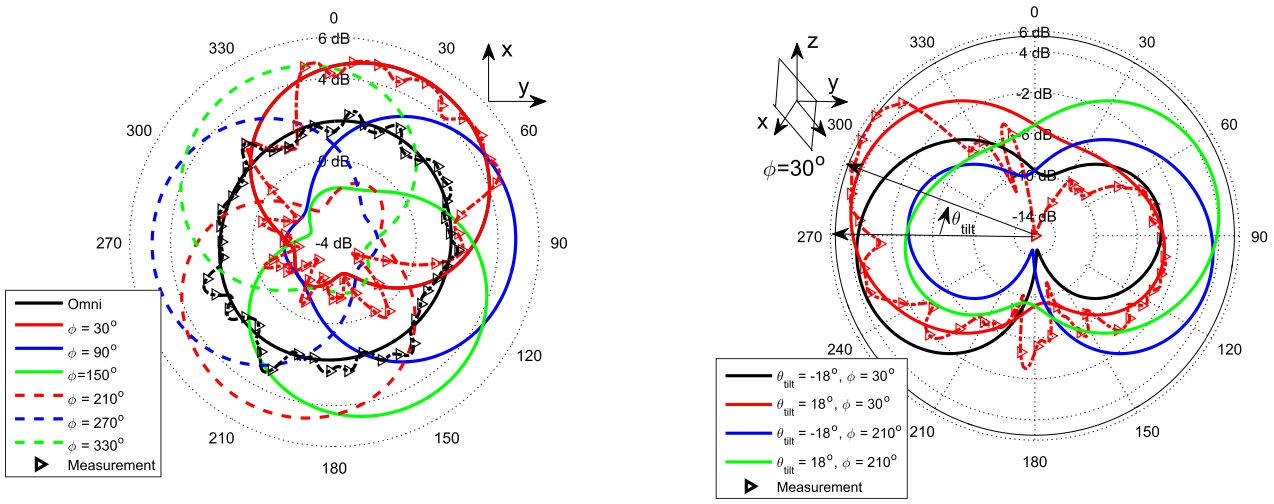

(a) (b)

Fig. 6. Realized gain pattern for the optimized RA at 5 GHz. (a) Omni-mode and different azimuth steering modes at (x, y)-plane ($\theta = 90°$) with beam-steering toward $\phi \in \{30°, 90°, \ldots, 330°\}$, along with measured patterns for omni-mode and azimuth steering mode at $\phi = 30°$. (b) Different elevation tilting modes at $\phi = 30°$ and $\phi = 210°$ planes, along with measured pattern for the elevation-tilt mode at $\theta_{\text{tilt}} = 18°$ and $\phi = 210°$, where θ_{tilt} is the elevation angle from x–y plane.

U_i, is modeled as described in [22] and [23]

$$h_{i,j}(\eta_j) = \sum_{p=1}^{P} c_{i,j} \langle \vec{G}_i(\Psi_p), T_p \vec{X}_j(\Omega_p; \eta_j) \rangle e^{j2\pi v_p t - f\tau_p} \quad (1)$$

where T_p is the 2×2 matrix representing the polarization leakage between the orthogonal polarization components of the E-field radiation, $\Psi_p = (\vartheta_p, \varphi_p)$ and $\Omega_p = (\theta_p, \phi_p)$ denote the angle-of-arrival and angle-of-departure, respectively, for the pth path, and $\vec{X}_j(\cdot)$ represents $\vec{B}_j(\cdot)$ for eNBs and $\vec{A}_{j-KS}$ for FAPs, respectively. The argument of $h_{i,j}(\eta)$ indicates the impact of underlying antenna mode to the channel gain with η denoting the antenna mode.

The average signal-to-interference plus noise ratio (SINR) at U_i being served by X_i is given by [24]

$$\rho_i(\boldsymbol{\mu}) = \frac{P_i g_{i,i}(\eta_i)}{\sum_{j\neq i} P_j g_{i,j}(\eta_j) + \sigma^2} \quad (2)$$

where $g_{i,j}(\eta_j) = E(|h_{i,j}(\eta_j)|^2)$ is the long-term channel power between U_i and X_j. The achievable rate at U_i is then

$$R_i(\boldsymbol{\mu}) = \log(1 + \rho_i(\boldsymbol{\mu})). \quad (3)$$

2) Combined Cell-Selection and RA Mode Optimization: Due to the availability of multiple RA modes at FAPs, signal-strength-based cell-selection schemes may fail to determine the proper serving station. This is mainly because the average signal-strength may significantly vary from one RA mode to another (e.g., front-to-back ratio of ∼7 dB as seen in Fig. 6) for a given UE. Here, we develop a utility-based cell- and mode-selection scheme that jointly determines the RA mode and served UEs at each access point. The proposed approach combines utility-optimization-based mode-selection with a biased cell selection scheme [25] where the serving cell j^* for U_i is decided using

$$j^* = \underset{j}{\text{argmax}}\, \delta_j P_j g_{i,j}(\eta_j) \quad (4)$$

with δ_j denoting the bias toward access station-j. We consider proportional fairness utility [26], which can be expressed as

$$\Upsilon(\boldsymbol{\mu}) = \sum_{j=1}^{KS+L} \sum_{i\in\mathcal{U}_j} \log\left(\frac{W}{|\mathcal{U}_j|} R_i(\boldsymbol{\mu})\right) \quad (5)$$

where W and $W_{j,i} = W/|\mathcal{U}_j|$ denote the total available bandwidth at each station X_j, and the bandwidth allocated for U_{j_i}, respectively.

We consider a distributed scheme where each FAP decides on its RA mode of operation locally. To that end, assume that each access point collects the signal quality measurements from nearby users. For example, in 3GPP LTE-A, a reference signal received power (RSRP) is evaluated at the users and fedback to the associated access station [27]. Let $\mathcal{V}_j$ denote the set of users whose signal measurements are available at access station-j. Note that, during cell-selection, F_j employs the signal measurements from UEs in $\mathcal{V}_j$.

The first KS and the last L terms in outer sum of (5) correspond to sum-log throughput from the eNBs and FAPs, respectively. Due to the relatively smaller transmit power levels and lower antenna gains at FAPs, the impact of RA mode variation over UEs served by eNBs is small. Therefore, the mode selection can focus on the utility due to FAPs. In addition, it is assumed that the aggregated interference from all access points onto user-i, i.e., the summation in the denominator of (2), is fixed ($\approx I_0$) for mode-selection purposes. Under these assumptions, substituting (2) and (3) in (5), applying Jensen's inequality on expected value of $\Upsilon(\boldsymbol{\mu})$, and after some

manipulations, we obtain the RA mode optimization at F_l as

$$\mu_l^* = \underset{\mu_l}{\text{argmax}} \sum_{i\in\mathcal{V}_l} \log\log\left(1+\frac{P_i g_{i,l}(\mu_l)}{I_0+\sigma^2}\right) + |\mathcal{V}_l|\log W - |\mathcal{V}_l|\log|\mathcal{V}_l|. \quad (6)$$

The optimization in (6) requires mode optimization for only a single FAP and over the UEs in the vicinity of this FAP.

Note that cell selection in (4) depends on the RA modes of FAPs. Some of the UEs appearing in the measurement list $\mathcal{V}_l$ of F_l may end up being served by another station due to the bias δ_j and the selected antenna mode at access station-j. Thus, the antenna mode selected at F_l under the assumption that all UEs in $\mathcal{V}_l$ would be served by this FAP may create significant interference to the UEs which are actually served by nearby access point. To combat this issue, one could extend the optimization in (6) over all nonempty subsets of $\mathcal{V}_l$. Here, we provide a low-complexity alternative solution to the exhaustive search approach. To that end, for each mode, let us sort the users in measurement list $\mathcal{V}_l$ in descending order according to the received signal qualities. Let $\{i_1,\ldots,i_{|\mathcal{V}_l|}\}$ indicate the UEs in the sorted set, with i_1 denoting the highest signal quality, and i_2 the second one, and so on. The joint optimization of RA modes along with the candidate served UEs can then be expressed as

$$\mu_l^* = \underset{\mu_l}{\text{argmax}} \max_{J} \sum_{j=1}^{J} \log\log\left(1+\frac{P_{i_j} g_{i_j,l}(\mu_l)}{I_0+\sigma^2}\right) + J\log W - J\log J. \quad (7)$$

Hence, the RA mode at F_l is selected such that those UEs in $\mathcal{V}_l$ contribute more to the local utility than the UEs receiving lower signal quality from this FAP, and thus avoid the off-loading of those UEs to the FAP for which the RA mode optimization do not get utility improvement.

3) Examples: Let us next investigate the performance of the parasitic RA and the proposed mode selection scheme in a wireless heterogenous cellular network. Table III summarizes the system level settings being used in this paper. We assume a hexagonal grid-based deployment and a wrap-around technique described in [28] to ensure accurate modeling of intercell and intracell interference. UEs are deployed according to the hot-spot scenario where a fraction of UEs are uniformly randomly dropped within a number of clusters that are also uniformly randomly created in the 57-cell area. Two FAP deployment scenarios are studied: 1) random deployment where FAPs are randomly dropped across the 57-cell area and 2) planned deployment where FAPs are dropped randomly within 50 m of the UE clusters. We employ the spatial channel model described by 3GPP in [23] and [29] targeted for performance evaluation of 5G networks. We extended this channel to the case of RAs that can assume different radiation patterns. The 3-D radiation patterns are obtained from full-wave analysis for various modes of operation as described in Section III (see Fig. 3). The cell selection and mode selection schemes use the RSRP calculation described in [23].

In Fig. 7, we compare the average capacity and coverage performance for various systems. For comparison purposes,

TABLE III
SYSTEM LEVEL SIMULATION PARAMETERS

Parameter	Value	Parameter	Value
Number of eNBs (K)	19	Number of sectors (S)	3
eNB-eNB distance	0.5 km	eNB antenna e-tilt	15^o (deg)
eNB antenna pattern	3D, sector antenna [23]	eNB antenna polarization	Vertical
eNB Tx Power	46 dBm	FAP Tx Power	30 dBm
eNB-UE channel	UMa [23]	FAP-UE channel	UMi [23]
UE deployment	Hot-spot (6 UEs/cluster)	Number of hot-spots	3 or 5 per sector
Number of UEs	1710 ($\sim$ 30/sector)	Number of FAPs	0, 3 or 5 per sector
UE antenna	Dipole	FAP antenna	RA with 24 modes
Cell selection bias	Optimized over 0, 3, 6 and 9 dB	RA modes	Diversity modes, Directive modes, Omni

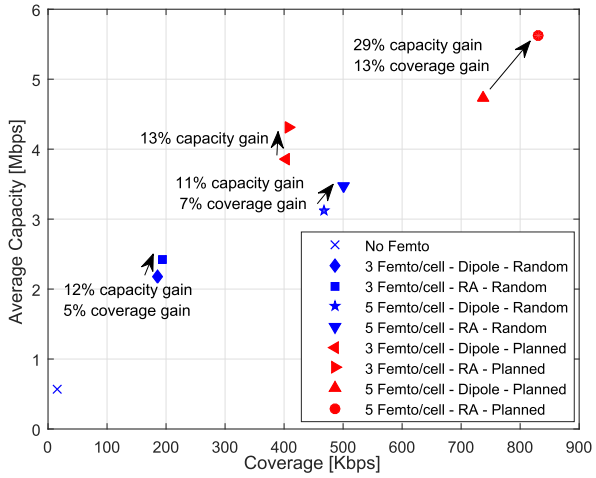

Fig. 7. Comparison of per UE capacity versus 5−percentile throughput coverage. For both planned and random deployment, FAPs with RAs provide performance improvement with distributed mode selection algorithm.

we include the case of no FAP in the system and the system with FAPs employing dipole antennas. The average capacity is defined as the average of 1710 UEs' Shannon rates evaluated using the resulting SINR values. For the coverage throughput, Γ_α, we set $\alpha = 0.05$, i.e., 5-percentile capacity coverage of the network. It is seen that in both planned and random FAP deployment, the RAs at FAPs provide significant capacity gains and coverage improvements. For example, in the planned deployment, the RA antennas provided an additonal 29% per UE percent capacity gain and 13% coverage improvement over the gains from small cell deployment employing dipole antennas. Even for randomly positioned FAPs, for which the FAPs are randomly dropped anywhere in the 57-sector area, the RA modes provide more than 10% capacity gains and 5% coverage improvements for both 3 and 5 FAP/sector. We note that in the simulations, omni-directional mode of operation is also included during mode selection optimization at FAPs. The omni-mode of operation becomes useful especially in random

FAP deployment scenarios where UEs may be uniformly distributed within the coverage area of the FAP.

V. Conclusion

A parasitic layer-based RA that is capable of 3-D beam-steering is developed and presented. This RA consists of a driven dipole antenna surrounded by a 3-D parasitic enclosure comprising of small metallic pixels interconnected by PIN diode switches. With different switch states, the geometry of the parasitic surfaces can be modified to create various radiation patterns. The RA geometry and the lumped components for switching circuitry are optimized to attain 360° azimuthal beam-steering and $-18°$ to 18° elevation tilts along with several diversity patterns. These resulting patterns can effectively be utilized for interference management in 5G wireless heterogeneous networks. The RA has been fabricated and its resonance characteristics and radiation patterns have been measured, which closely matched to full-wave analysis results. Assuming a typical 5G heterogeneous network, where the small cell access points are equipped with the presented RA, a distributed low-complexity mode selection algorithm is developed. Using the system level performance evaluation methodology of 5G networks by 3GPP, the capacity and coverage performance is studied. It is seen that up to 29% throughput gains and 13% coverage improvements can be attained. This paper attempts to develop a unified approach with the goal of achieving 5G performance requirements, where antenna design, communications and network aspects are seamlessly integrated, and the critical system parameters (environment, EM wave properties, and communication algorithms) are jointly optimized.

This single-element RA is capable of creating desirable directive beam patterns in both the azimuthal and elevation planes. An immediate future research direction is to extend this architecture to the case of reconfigurable MIMO antenna systems. Furthermore, other pixel shapes and parasitic enclosure geometries can be investigated to create polarization diverse patterns in addition to directionally diverse patterns. From our system level performance results, we see that the presented RA has also significant consequences for the design and optimization of 5G and beyond networks. For example, interference management, load balancing, and RA mode design/selection can jointly be optimized to excel the 5G network performance.

References

[1] *IMT Vision—Framework and Overall Objectives of the Future Development of IMT for 2020 and Beyond*, document Rec. ITU-R m.2083-0, ITU-R (Radiocomunication Sector of ITU), Sep. 2015. [Online]. Available: https://www.itu.int/dms_pubrec/itur/rec/m/R-REC-M.2083-0-201509-I!!PDF-E.pdf

[2] J. Bernhard, *Reconfigurable Antennas* (Synthesis Lectures on Antennas and Propagation Series). San Rafael, CA, USA: Morgan & Claypool, 2007.

[3] D. Rodrigo, B. A. Cetiner, and L. Jofre, "Frequency, radiation pattern and polarization reconfigurable antenna using a parasitic pixel layer," *IEEE Trans. Antennas Propag.*, vol. 62, no. 6, pp. 3422–3427, Jun. 2014.

[4] D. Piazza, N. Kirsch, A. Forenza, R. Heath, and K. Dandekar, "Design and evaluation of a reconfigurable antenna array for MIMO systems," *IEEE Trans. Antennas Propag.*, vol. 56, no. 3, pp. 869–881, Mar. 2008.

[5] Z. Li, D. Rodrigo, L. Jofre, and B. A. Cetiner, "A new class of antenna array with a reconfigurable element factor," *IEEE Trans. Antennas Propag.*, vol. 61, no. 4, pp. 1947–1955, Apr. 2013.

[6] D. Rodrigo and L. Jofre, "Frequency and radiation pattern reconfigurability of a multi-size pixel antenna," *IEEE Trans. Antennas Propag.*, vol. 60, no. 5, pp. 2219–2225, May 2012.

[7] B. A. Cetiner, H. Jafarkhani, J.-Y. Qian, H. J. Yoo, A. Grau, and F. D. Flaviis, "Multifunctional reconfigurable MEMS integrated antennas for adaptive MIMO systems," *IEEE Commun. Mag.*, vol. 42, no. 12, pp. 62–70, Dec. 2004.

[8] X. Yuan *et al.*, "A parasitic layer-based reconfigurable antenna design by multi-objective optimization," *IEEE Trans. Antennas Propag.*, vol. 60, no. 6, pp. 2690–2701, Jun. 2012.

[9] H. Kawakami and T. Ohira, "Electrically steerable passive array radiator (ESPAR) antennas," *IEEE Antennas Propag. Mag.*, vol. 47, no. 2, pp. 43–50, Apr. 2005.

[10] A. Kalis, A. Kanatas, and C. Papadias, *Parasitic Antenna Arrays for Wireless MIMO Systems* (SpringerLink: Bücher). New York, NY, USA: Springer, 2013. [Online]. Available: http://www.springer.com/us/book/9781461479987#aboutBook

[11] C. Sun, A. Hirata, T. Ohira, and N. C. Karmakar, "Fast beamforming of electronically steerable parasitic array radiator antennas: Theory and experiment," *IEEE Trans. Antennas Propag.*, vol. 52, no. 7, pp. 1819–1832, Jul. 2004.

[12] B. Alshami, H. Aboulnour, and M. Dib, "Design of a broadband espar antenna," in *Proc. Medit. Microw. Symp. (MMS)*, Nov. 2009, pp. 1–6.

[13] R. Schlub and D. V. Thiel, "Switched parasitic antenna on a finite ground plane with conductive sleeve," *IEEE Trans. Antennas Propag.*, vol. 52, no. 5, pp. 1343–1347, May 2004.

[14] *Study on Elevation Beamforming/Fulldimension (FD) Multiple Input Multiple Output (MIMO) for LTE (Rel. 13)*, document TR 36.897, 3GPP, Jun. 2015. [Online]. Available: http://www.3gpp.org/ftp/Specs/archive/36_series/36.897/36897-d00.zip

[15] H. Halbauer, S. Saur, J. Koppenborg, and C. Hoek, "3D beamforming: Performance improvement for cellular networks," *Bell Labs Tech. J.*, vol. 18, no. 2, pp. 37–56, Sep. 2013.

[16] ANSYS. (2016). *ANSYS HFSS, Version 16.0*. [Online]. Available: http://www.ansys.com

[17] C. A. Balanis, *Antenna Theory: Analysis and Design*. Hoboken, NJ, USA: Wiley, 2005.

[18] Z. Li, E. Ahmed, A. M. Eltawil, and B. A. Cetiner, "A beam-steering reconfigurable antenna for WLAN applications," *IEEE Trans. Antennas Propag.*, vol. 63, no. 1, pp. 24–32, Jan. 2015.

[19] D. Cheng and C. Chen, "Optimum element spacings for Yagi-Uda arrays," *IEEE Trans. Antennas Propag.*, vol. AP-21, no. 5, pp. 615–623, Sep. 1973.

[20] H. S. Dhillon, R. K. Ganti, F. Baccelli, and J. G. Andrews, "Modeling and analysis of K-tier downlink heterogeneous cellular networks," *IEEE J. Sel. Areas Commun.*, vol. 30, no. 3, pp. 550–560, Apr. 2012.

[21] *Scenarios and Requirements for Small Cell Enhancements for E-UTRA and E-UTRAN (Rel. 13)*, document TR 36.932, 3GPP, Dec. 2015. [Online]. Available: http://www.3gpp.org/ftp/Specs/archive/36_series/36.932/36932-d00.zip

[22] C. Oestges and B. Clerckx, *MIMO Wireless Communications: From Real-World Propagation to Space-Time Code Design*. New York, NY, USA: Elsevier, 2010.

[23] *Study on 3D Channel Model for LTE (Rel. 12)*, document TR 36.873, 3GPP, Jun. 2015. [Online]. Available: http://www.3gpp.org/ftp/Specs/archive/36_series/36.873/36873-c20.zip

[24] S. Mukherjee, "Distribution of downlink sinr in heterogeneous cellular networks," *IEEE J. Sel. Areas Commun.*, vol. 30, no. 3, pp. 575–585, Apr. 2012.

[25] A. K. Gupta, H. S. Dhillon, S. Vishwanath, and J. G. Andrews, "Downlink multi-antenna heterogeneous cellular network with load balancing," *IEEE Trans. Commun.*, vol. 62, no. 11, pp. 4052–4067, Nov. 2014.

[26] N. Prasad, M. Arslan, and S. Rangarajan, "Exploiting cell dormancy and load balancing in LTE HetNets: Optimizing the proportional fairness utility," *IEEE Trans. Commun.*, vol. 62, no. 10, pp. 3706–3722, Oct. 2014.

[27] E. Dahlman, S. Parkvall, and J. Skold, *4G: LTE/LTE-Advanced for Mobile Broadband*, New York, NY, USA: Elsevier, 2013.

[28] X. Chu, D. López-Pérez, Y. Yang, and F. Gunnarsson, *Heterogeneous Cellular Networks: Theory, Simulation and Deployment*. Cambridge, U.K.: Cambridge Univ. Press, 2013.

[29] *Study on New Radio (NR) Access Technology Physical Layer Aspects (Rel. 14)*, document Draft for TR 38.802, 3GPP, Oct. 2016, [Online]. Available: http://www.3gpp.org/ftp/TSG_RAN/WG1_RL1/TSGR1_86b/Docs/R1-1610848.zip

Mohammad Ababil Hossain received the B.Sc. and M.Sc. degrees in electrical and electronic engineering from the Bangladesh University of Engineering and Technology, Dhaka, Bangladesh, in 2012 and 2015, respectively, and the M.S.E.E. degree from Utah State University, Logan, UT, USA, in 2017.

He is currently a Senior Antenna Engineer with i5 Technologies, Inc., Logan, UT, USA. His current research interests include analytical electromagnetic modeling, antennas, RF circuits, optics, and metamaterials.

Israfil Bahceci (S'01–M'06) received the B.S. degree in electrical engineering from Bilkent University, Ankara, Turkey, in 1999, the M.S. degree in electrical engineering from Arizona State University, Tempe, AZ, USA, in 2001, and the Ph.D. degree in electrical engineering from the Georgia Institute of Technology, Atlanta, GA, USA, in 2005.

He is currently a Research Scientist with the Department of Electrical and Computer Engineering, Utah State University, Logan, UT, USA, and is also a Vice President for Research and Development with i5 Technologies, Inc., Logan, UT, USA. He was a Post-Doctoral Fellow with the University of Waterloo, Waterloo, ON, Canada, from 2005 to 2007. He was a Research and Development Engineer with Nortel Networks, Canada, from 2007 to 2009. He was with Huawei Technologies, Canada, from 2009 to 2011. He was with the TOBB University of Economics and Technology, Ankara, Turkey, from 2011 to 2015. His current research interests include systems, with a particular focus on communication and signal processing, wireless and mobile communications, distributed estimation/detection, and reconfigurable antenna systems for 5G and beyond systems.

Bedri A. Cetiner (M'99) received the Ph.D. degree in electronics and communications engineering from Yildiz Technical University, Istanbul, Turkey, in 1999.

He is currently a Professor with the Department of Electrical Engineering, Utah State University, Logan, UT, USA.. From 1999 to 2000, he was a NATO Science Fellow with the University of California, Los Angeles, CA, USA. He was with the Department of Electrical Engineering and Computer Science, University of California, Irvine, CA, USA, where he was a Research Scientist from 2000 to 2004. From 2004 to 2007, he was an Assistant Professor with the Department of Space Science and Engineering, Morehead State University, Morehead, KY, USA. In 2007, he joined Utah State University. He is currently the Principal Inventor of nine patented technologies including microwave laminate compatible RF MEMS technology and MRA equipped multi-input multi-output (MIMO) systems and is also the Founder, President, and CEO of i5 Technologies Inc., Logan, UT, USA. His current research interests include applications of micronano technologies to a new class of micro-/millimeter-wave circuits and systems, and intelligent wireless communications systems with an emphasis on the multifunctional reconfigurable antennas for use in cognitive MIMO systems.

Prof. Cetiner is a member of the IEEE Antennas and Propagation, Microwave Theory and Techniques, and Communication Societies.